

Validation of the nonhydrostatic General Curvilinear Coastal Ocean Model (GCCOM) for stratified flows[☆]

Mariangel Garcia^{a,*}, Paul F. Choboter^b, Ryan K. Walter^c, Jose E. Castillo^a

^a Computational Science Research Center, San Diego State University, 5500 Campanille Drive, San Diego, CA 92118, United States

^b Mathematics Department, California Polytechnic State University, San Luis Obispo, CA 93407-0403, United States

^c Physics Department, California Polytechnic State University, San Luis Obispo, CA 93407-0403, United States

ARTICLE INFO

Keywords:

Nonhydrostatic
GCCOM
Stratified flows
Lock exchange
Internal seiche
Internal waves beam generation
Benchmark
Gravity-driven flows

ABSTRACT

While global- and basin-scale processes can be captured quite well with computationally-inexpensive hydrostatic models, smaller-scale features such as shoaling nonlinear internal waves and bores, coastal fronts, and other convective processes require the use of a nonhydrostatic model to accurately capture dynamics. Here the nonhydrostatic capabilities of the General Curvilinear Coastal Ocean Model (GCCOM) in a stratified environment are introduced. GCCOM is a three-dimensional, nonhydrostatic Large Eddy Simulation (LES), rigid lid model that has the ability to run in a fully three-dimensional general curvilinear coordinate system. This model was previously validated for unstratified flows with curvilinear coordinates. Here, recent advances of the model to simulate stratified flows are presented, focusing on sigma coordinate grids with both flat bottom geometry and a local gently sloping seamount. In particular, a suite of test cases widely used as benchmarks for assessing the nonhydrostatic capabilities for gravity-driven flows and internal waves is presented: an internal seiche in a flat bottom tank, the classic lock release and gravity current experiment, and a field-scale internal wave beam experiment consisting of an oscillating tidal flow over a topographic ridge. GCCOM shows excellent agreement with the benchmark test cases and is able to accurately resolve complex nonhydrostatic phenomena in stratified flows. Future studies will utilize the model capabilities for realistic field-scale internal wave simulations.

1. Introduction

One of the major challenges in the simulation of coastal ocean dynamics is the vast range of length and time scales present. While global- and basin-scale processes and currents can be captured quite well with computationally-inexpensive hydrostatic models (e.g., [1]), smaller-scale features such as shoaling nonlinear internal waves and bores, coastal fronts, and other convective processes require the use of a nonhydrostatic model to accurately capture dynamics [2–6]. More formally, for processes where the characteristic frequency (e.g., of an internal wave) is comparable to the buoyancy frequency for a stratified fluid, or when the characteristic vertical length scale is comparable to the horizontal length scale, nonhydrostatic effects cannot be neglected (e.g., [7]). This is particularly true for simulations that aim to capture the multi-

scale internal wave energy cascade, a process that has wide ranging effects on the physical and biological environment [8–16].

Simulating nonhydrostatic processes is computationally expensive, as these models require an elliptic solver for the dynamic pressure [17,3,18]. Moreover, for internal wave simulations, a high horizontal grid resolution is required (i.e., small grid lepticity) so that numerically-induced dispersion is small relative to physical dispersion [19]. However, with vast improvements in computing power and computational methods, the use of nonhydrostatic ocean models has become increasingly popular over the last decade [20–25,7,26–30,5,31–33,6].

Key features of a subset of these models are summarized in Table 1. Among others, a distinguishing feature between the models is the coordinate system used. The Massachusetts Institute of Technology Global Circulation Model (MITgcm [29]) uses a curvilinear grid in the horizontal coordinates, and z-coordinates in the vertical with a finite-volume treatment of irregular bathymetry; the Bergen Ocean Model (BOM, Berntsen et al. [22]) uses mode splitting and sigma-coordinates with finite differences on a staggered grid; the Regional Ocean Modeling System (ROMS [7]) variant with nonhydrostatic capabilities (not openly available via ROMS community web-page) uses sigma coordinates, as well as the Finite Volume

[☆] The model data generated in this study are available at <http://dolphin.sdsu.edu:8080/web-data/publ.3.2018/>.

* Corresponding author.

E-mail addresses: mvgarcia@sdsu.edu (M. Garcia), pchobote@calpoly.edu (P.F. Choboter), rkwalter@calpoly.edu (R.K. Walter), jcastillo@sdsu.edu (J.E. Castillo).

Table 1
Key features of select nonhydrostatic ocean models.

Models	MITgcm	SUNTANS	ROMS-NH	FVCOM-NH	SOMAR	GCCOM
Author, Year	Marshall et al. [29]	Fringer et al. [25]	Kanarska et al. [7]	Lai et al. [27]	Chalamalla et al. [24]	Present article
Equations	NSE RANS	NSE LES	NSE	NSE	NSE	NSE LES
Horizontal grid	Orthogonal curvilinear	Unstructured	Curvilinear	Unstructured	Curvilinear	Curvilinear
Vertical coordinate system	z–	z–	σ –	Generalized σ –	Curvilinear	Curvilinear
Grid type	Arakawa C-grid	Triangular grid	Arakawa C-grid	Triangular grid	AMR C-grid	Arakawa C-grid
Spatial discretization scheme	Finite volume	Finite volume	Finite volume	Finite volume	Finite volume	Finite difference
Time discretization scheme	Quasi 2nd Adams-Bashforth	Adams-Bashforth	Split-Explicit	Modified RK4/ Semi-Implicit	PPM/Semi-implicit	RKW3
Pressure solution method	Fractional step	Pressure-Split	Fractional step	Fractional step	Fractional step	Fractional step
Pressure solver	Conjugate-Gradient (CG)	CG	PCG,GMRES	Multigrid (MG)	Leptic method/MG	MG or Block-Jacobi
Library dependency	None	ParaMetis	PetSC with Hypre	ParaMetis	CHOMBO	AGMG, PetSC
Program language	F90	C	F90	F90	C++/F77	F90

Coastal Ocean Model (FVCOM [27]); the Stanford Unstructured Nonhydrostatic Terrain-following Adaptive Navier-Stokes Simulator (SUNTANS [25]) employs an unstructured grid in the horizontal and z-level in the vertical; Koltakov and Fringer [26] presented a moving grid method using generalized curvilinear coordinates; and the Stratified Ocean Model with Adaptive Refinement (SOMAR [5]) features adaptive mesh refinement and more recently an LES component [24].

Here, the capabilities of the nonhydrostatic General Curvilinear Coastal Ocean Model (GCCOM) for stratified flows are introduced. GCCOM is a three-dimensional large eddy simulation (LES) Navier–Stokes solving model that has the ability to run in a fully three-dimensional general curvilinear coordinate system. Earlier versions of this model were described by Abouali and Castillo [20], Torres [34], Torres et al. [35], Torres and Castillo [36], Torres et al. [37] for flow over complex terrain; however, these earlier versions treated stratification with a simplified buoyancy forcing term and did not explicitly take into account hydrostatic pressure gradients. The version of the model described here computes the density effects by removing the buoyancy term and adding a horizontal pressure gradient force that arises from the hydrostatic component of pressure following Shchepetkin and McWilliams [38]. This representation, which is described further below, has been shown to accurately capture gravity-driven flows and internal waves. Furthermore, to lower the computational cost of the nonhydrostatic pressure, two libraries were integrated: the Aggregation-based Algebraic MultiGrid library (AGMG [39]) and the Portable, Extensible Toolkit for Scientific Computation (PetSC [40]) a comparison of the efficiency of these libraries in GCCOM is presented in Valera et al. [41]. GCCOM has also demonstrated the ability to nest within a regional hydrostatic model, allowing for the efficient simulation of multiscale processes [42], and it also includes a data assimilation framework [43].

In this contribution, we focus on the validation of the nonhydrostatic capabilities of the model in a stratified environment. In particular, a suite of test cases widely used as benchmarks for assessing the nonhydrostatic capabilities for gravity-driven flows and internal waves are used. Details of the model, including the equations and numerical methods, are described in Section 2. The numerical experiments (Section 3) follow and include an internal seiche (Section 3.1), a lock release (Section 3.2), and a tidally-forced stratified flow over a seamount aimed at investigating the formation of internal wave beams (Section 3.3). These results collectively demonstrate the accuracy of GCCOM for these types of flows.

2. Governing equations

2.1. Equations of motion

GCCOM solves the three-dimensional Navier–Stokes equations with the Boussinesq approximation, assuming nondivergent flow,

a rigid lid at the ocean surface, and a Large Eddy Simulation (LES) formulation with a subgrid-scale model. A complete description of the equations used in GCCOM was presented by Abouali and Castillo [20]. In this section, an overview of the model in physical space is presented in order to document the new implementation of horizontal pressure gradient force, which allows the model to accurately simulate stratified and gravity-driven flows. Detailed information about the curvilinear transformation and discretizations can be found in . The equations of motion are,

$$\frac{\partial \mathbf{u}}{\partial t} + \mathbf{u} \cdot \nabla \mathbf{u} = -\frac{1}{\rho_0} \nabla p - \frac{g\rho}{\rho_0} \mathbf{k} - \nabla \cdot \boldsymbol{\tau}, \quad (1)$$

$$\frac{\partial T}{\partial t} + \mathbf{u} \cdot \nabla T = \nabla \cdot (k_T \nabla T), \quad (2)$$

$$\frac{\partial S}{\partial t} + \mathbf{u} \cdot \nabla S = \nabla \cdot (k_S \nabla S), \quad (3)$$

$$\nabla \cdot \mathbf{u} = 0, \quad (4)$$

and

$$\rho = f(T, S, p), \quad (5)$$

where $\mathbf{u} = (u, v, w)$ is the velocity vector, $g\rho\mathbf{k}/\rho_0$ represents the acceleration due to gravity, $\boldsymbol{\tau}$ represents the stress tensor computed with a subgrid-scale model, T is temperature, S is salinity, k_T is the temperature diffusivity, k_S is the salinity diffusivity, and f is an equation of state. Note in particular that the pressure p is not assumed to be hydrostatic. This model employs the rigid-lid approximation.

The sub-grid stress tensor, τ_{ij} , is calculated using the Smagorinsky model [44],

$$\tau_{ij} = -2\nu_T e_{ij}, \quad \nu_T = (C_S l)^2 \sqrt{2e_{ij}e_{ij}}, \quad e_{ij} = \frac{1}{2} \left(\frac{\partial u_i}{\partial x_j} + \frac{\partial u_j}{\partial x_i} \right),$$

where ν_T is the turbulent eddy viscosity and e_{ij} is the strain rate tensor. The length scale is $l = (\Delta x \Delta y \Delta z)^{1/3}$, where Δx , Δy , and Δz are the discretized grid step size in the x , y , and z directions, respectively. Physically relevant values of the Smagorinsky constant C_S are 0.08–0.22 [45].

For the experiments described here, the equation of state is taken to be a linear function of temperature and salinity,

$$\rho = f(T, S) = \rho_0 (1 - \alpha(T - T_0) + \beta(S - S_0)), \quad (6)$$

where $\rho_0 = 1027 \text{ kg m}^{-3}$, $T_0 = 10^\circ \text{C}$, $S_0 = 35$, $\alpha = 1.664 \times 10^{-4} \text{ }^\circ \text{C}^{-1}$, and $\beta = 7.605 \times 10^{-4}$ [46]. The linear equation of state is used for the simulations described here to facilitate close comparison of the numerical product with theoretical results, which are described in terms of density values. GCCOM has the capability to employ the fully nonlinear UNESCO equation of state.

2.2. Numerical methods

In order to perform calculations on three-dimensional arbitrarily (orthogonal and non-orthogonal) shaped geometries, generalized independent variables are introduced, which transform the equations of motion from physical coordinates into general curvilinear coordinates [36] (see Appendix A). One of the advantages of a curvilinear grid with a uniformly applied coordinate transformation is the ease of the application of the boundary conditions, as well as the ability to solve the transformed equation on the computational grid which is more efficient for high-performance computing since the computational grid maps the computer. Central finite differences are used to calculate the metrics of transformation, except at the boundaries, where one-sided second order accurate finite differences are used [20] (see Appendix B). In the computational coordinates, derivatives are approximated using a second-order finite-difference scheme, with central differences used for the linear terms, and the Kawamura method (4th-order accurate) for the nonlinear advection terms [47].

The time discretization is based on the fractional step method of Kim and Moin [48] and employs the third-order Runge–Kutta method described by Wicker and Skamarock [49]. The horizontal pressure gradient force arising from the hydrostatic part of the pressure p_H is computed explicitly (see Section 2.3 for details). First, the density field is calculated at time step n using the equation of state,

$$\rho^n = f(T^n, S^n). \quad (7)$$

Then the hydrostatic pressure gradient $\nabla_H p_H$ is calculated following the methods outlined in Section 2.3, where $\nabla_H = (\partial/\partial x, \partial/\partial y)$ is the gradient in only the horizontal components, so that $\nabla_H p_H$ is zero in the w -momentum equation. Following this, a predicted velocity field \mathbf{u}^* is computed using the hydrostatic pressure gradient,

$$\mathbf{u}^* = \text{RK3} \left(-\mathbf{u}^n \cdot \nabla \mathbf{u}^n - \frac{1}{\rho_0} \nabla_H p_H - \nabla \cdot \boldsymbol{\tau}^n \right), \quad (8)$$

where RK3() denotes the application of the third-order Runge–Kutta method of Wicker and Skamarock [49]. Next, a correction to the pressure field p_c is computed to ensure a divergence-free velocity field,

$$\nabla^2 p_c = \frac{1}{\Delta t} \nabla \cdot \mathbf{u}^*, \quad (9)$$

assuming no-gradient boundary conditions for p_c , from which a corrected velocity field is calculated at time step $n+1$,

$$\mathbf{u}^{n+1} = \mathbf{u}^* - \Delta t \nabla p_c. \quad (10)$$

The Laplacian transformation of p_c (Eq. (9)) in curvilinear coordinates can be found in Appendix C. Temperature and salinity are updated as follows:

$$T^{n+1} = \text{RK3} \left(-\mathbf{u}^{n+1} \cdot \nabla T^n + \nabla \cdot (k_T \nabla T^n) \right), \quad (11)$$

$$S^{n+1} = \text{RK3} \left(-\mathbf{u}^{n+1} \cdot \nabla S^n + \nabla \cdot (k_S \nabla S^n) \right). \quad (12)$$

2.3. Hydrostatic pressure gradient

The discretization of the hydrostatic pressure gradient is similar to the scheme as described by Shchepetkin and McWilliams [38]. Since hydrostatic pressure is defined by

$$\frac{\partial p_H}{\partial z} = -g\rho, \quad (13)$$

it follows that

$$\frac{\partial p_H}{\partial x} = \frac{\partial}{\partial x} \int_z^0 g\rho d\tilde{z} = \int_z^0 g \frac{\partial \rho}{\partial x} d\tilde{z}, \quad (14)$$

where $z=0$ is at the ocean surface, and $z<0$ in the interior. In GCCOM, $\partial\rho/\partial x$ and $\partial\rho/\partial y$ are computed at each grid point on the curvilinear grid using the same finite difference algorithm as spatial derivatives of other terms in the model [36,20]. To evaluate the integral in (14), a cubic spline is constructed for each of $\partial\rho/\partial x$ and $\partial\rho/\partial y$, according to

$$f(\xi) = f^{(0)} + f^{(1)}\xi + f^{(2)}\frac{\xi^2}{2} + f^{(3)}\frac{\xi^3}{3!}, \quad (15)$$

where $0 < \xi < 1$ is a local computational coordinate between two vertical grid points. The coefficients are given by

$$\begin{aligned} f^{(0)} &= f_k, \quad f^{(1)} = d_k, \quad f^{(2)} = (6\Delta_k - 2d_k - 4d_k)/h, \quad f^{(3)} \\ &= (6d_k + 6d_{k+1} - 12\Delta_k)/h^2, \end{aligned} \quad (16)$$

where $h = z_{k+1} - z_k$ is the local change in vertical coordinate and $\Delta_k = (f_{k+1} - f_k)/h$. Here, f_k represents the value of $\partial\rho/\partial x$ or $\partial\rho/\partial y$ at $\xi = 0$ and f_{k+1} is the same function at $\xi = 1$. The parameter d_k is computed as in Shchepetkin and McWilliams [38] to reduce spurious oscillations,

$$d_k = \begin{cases} \frac{2\Delta_k \Delta_{k-1}}{\Delta_k + \Delta_{k-1}} & \text{if } \Delta_k \Delta_{k-1} > 0, \\ 0 & \text{otherwise.} \end{cases} \quad (17)$$

The cubic spline (15) is integrated vertically to evaluate $\partial p_H/\partial x$ and $\partial p_H/\partial y$ at the cell centers of the staggered grid. The final steps of the calculation are an interpolation of $\partial p_H/\partial x$ from the center grid to the u -grid, and an interpolation of $\partial p_H/\partial y$ from the center grid to the v -grid.

3. Nonhydrostatic stratified test cases

3.1. Internal seiche

The first test case that explores the nonhydrostatic capabilities of GCCOM is that of a two layer internal seiche with various interface thicknesses. This test case is similar to the two-dimensional free-surface internal seiche test cases of Casulli [2] and Fringer et al. [25], except that GCCOM is run in three dimensions with free slip boundary conditions in the lateral direction and a rigid lid. Following Kundu [50], the linearized dispersion relation for a small-amplitude internal seiche with two layers separated by an interface with finite thickness is given by

$$\omega^2 = \frac{g'k}{2} \tanh\left(\frac{kD}{2}\right) f(k\delta), \quad (18)$$

where $k = 2\pi/\lambda_w$ is the wave number, which is determined by length of the domain L and the fundamental wavelength $\lambda_w = 2L$; $g' = g\Delta\rho/\rho_0$ is the reduced gravity; g is the magnitude of the acceleration due to gravity; D is the domain depth; δ is the interface thickness; and $f(k\delta) = (1 + k\delta/2)^{-1}$ represents the effect of the finite-width interface. Dividing both sides of Eq. (18) by k^2 yields an expression for the phase speed squared, which can be used to calculate the speed of the leftward and rightward propagating waves that superpose to yield the standing wave (i.e., the internal seiche),

$$c^2 = \frac{g'}{2k} \tanh\left(\frac{kD}{2}\right) f(k\delta). \quad (19)$$

The shallow ($kD \rightarrow 0$) and deep ($kD \rightarrow \infty$) water limits of Eq. (19) are investigated. In the shallow water limit, the phase speed is only a function of depth and reverts to the shallow-water wave speed (assuming the dispersive character of the finite interface thickness is negligible [25]), whereas in the deep water limit, the phase speed

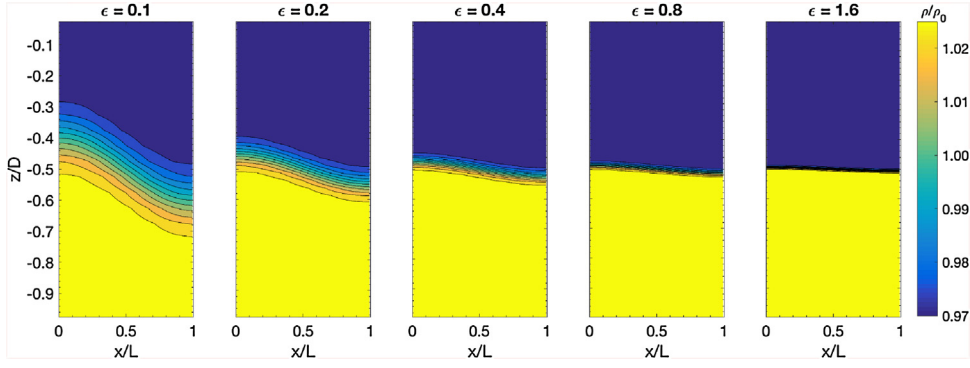


Fig. 1. Initial normalized density field of the internal seiche for the various aspect ratios.

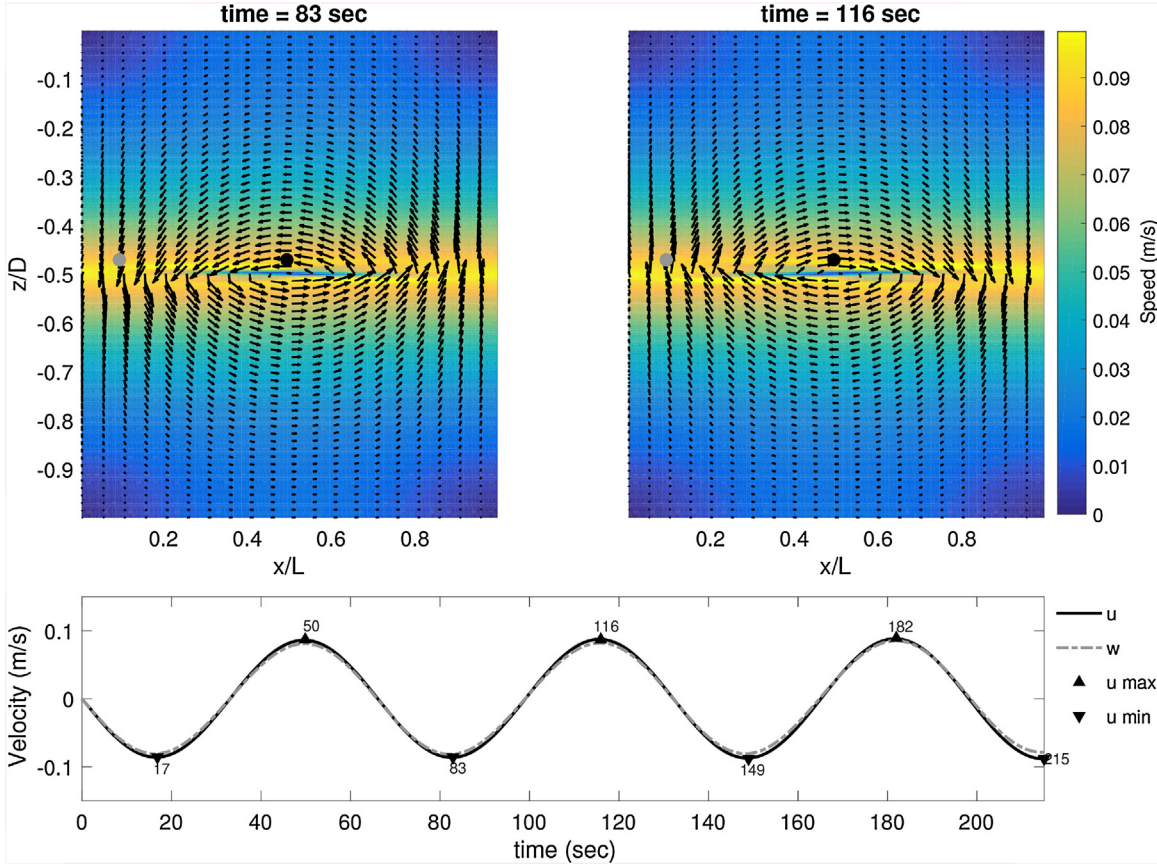


Fig. 2. Example horizontal velocity u fields of the internal seiche experiment at the minimum (left) and maximum (right) horizontal velocity for $\epsilon = 1.6$ at plane $Y = L/2$. The insets show the velocity over time for both the horizontal (u) and vertical (w) velocities at a location slightly above the center of the domain (black dot in top panel).

becomes independent of depth. A comparison of Eq. (19) to the deep water phase speed yields

$$\left(\frac{c}{c_{dw}}\right)^2 = \frac{\frac{g'}{2k} \tanh\left(\frac{kD}{2}\right) f(k\delta)}{\frac{g'}{2k} f(k\delta)} = \tanh\left(\frac{\pi\epsilon}{2}\right), \quad (20)$$

where $\epsilon = D/L$ is the aspect ratio of the standing wave specified by the size of the domain. As the aspect ratio decreases, and horizontal length of the domain becomes much larger than the vertical extent ($\epsilon \ll 1$), the waves are not expected to become frequency-dispersive and the wave speed will approach the shallow-water wave speed. For cases where the horizontal extent of the domain is on the order of the vertical extent ($\epsilon = O(1)$), the waves will become frequency dispersive and approach the deep-water wave speed. Given that the frequency-dispersive behavior of internal gravity

waves is a nonhydrostatic effect, the aspect ratio can be used as a measure of the nonhydrostasy in this test case.

The model was set up on an equally spaced Cartesian grid with a horizontal length $L = 100$ m and a horizontal grid spacing of $\Delta x = 1$ m. In order to vary the aspect ratio, and hence the nonhydrostasy, the model was run at the following depths with a vertical grid resolution of 0.5 m: 10, 20, 40, 80, and 160 m (representing $\epsilon = 0.1, 0.2, 0.4, 0.8$, respectively). The simulation was run for a total of 250 s with a time step of $\Delta t = 0.001$ s. Free-slip boundary conditions were employed along all wall boundaries.

For the experiments with varying depths (aspect ratios), the initial density stratification is given as in Fringer et al. [25],

$$\rho(x, y, z, t = 0) = -\frac{\Delta\rho}{2} \tanh\left[\frac{2 \tanh^{-1} \alpha_s}{\delta} \left(z + \frac{D}{2} - a \cos(kx)\right)\right]. \quad (21)$$

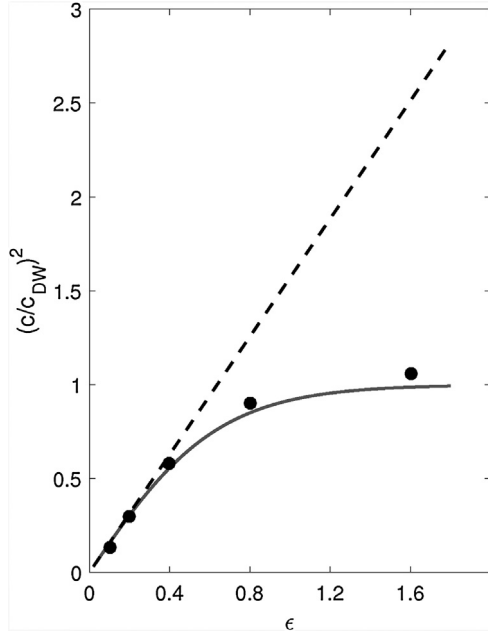


Fig. 3. Ratio of the nonhydrostatic wave speed to the deep-water wave speed as a function of the aspect ratio for both the model results (circles), as well as what theory predicts (solid line). The dashed line denotes the ratio of the shallow-water wave speed to that of the deep-water wave speed (cf. [3]).

where $\Delta\rho/\rho_0=0.06$ represents the normalized difference in density between the top and bottom layers, $a=1$ m is the seiche-amplitude, $\delta=5$ m, and $\alpha_s=0.99$. The initial density profiles for each numerical experiment are shown in Fig. 1.

The modeled wave speed was calculated by first determining the period of oscillation T by looking at the time series of the horizontal velocity u over time at a particular point near the center of the domain (Fig. 2). The wave speed was then calculated from $c = \frac{\omega}{k} = \frac{2\pi}{kT}$, where $k = \frac{2\pi}{\lambda_w} = \frac{\pi}{L}$ is determined from the length of the domain. The modeled wave speed was compared to the theoretical deep-water (i.e., nonhydrostatic) wave speed given by Eq. (19). Fig. 3 shows the ratio of the nonhydrostatic wave speed to the deep-water wave speed (denominator of Eq. (20)) for the both the model results (open circles), as well as what theory predicts (solid line, Eq. (20)). GCCOM accurately captures the wave speed for large aspect ratios, where nonhydrostatic effects are expected to be large. Slight differences are likely due to using a linearized dispersion relation and a finite-interface. Moreover, the velocity field in Fig. 2 for $\epsilon=1.6$ (highly nonhydrostatic) is able to accurately capture the decrease in magnitude of the velocity vectors away from the internal interface, a phenomena that would not be present in a hydrostatic solver where the waves would behave like shallow water waves with. The decay away from the interface can also be seen in the vertical profile of the horizontal velocity in Fig. 4. This profile, as well as the vertical velocity profile, match the shape of the linearized eigenfunctions shown in Fringer and Street [51]. These results demonstrate that the model is able to accurately capture the frequency-dispersive nature and key nonhydrostatic characteristics of the internal seiche.

3.2. Lock exchange flow

The second validation experiment performed was the classic lock exchange (also called lock release) problem, where two fluids with different densities are initially separated by a wall that is later released. This test case follows a similar numerical setup to the three-dimensional direct numerical simulations (DNS) of Härtel et al. [52], the two-dimensional simulation of Fringer et al. [25]

using SUNTANS, and the two-dimensional simulation of Lai et al. [27] using FVCOM-NH. The simulation is performed in a three-dimensional domain ($401 \times 6 \times 101$) with a tank of length $L_x=0.8$ m, a lateral width of $L_y=0.01$ m, and a depth $D=0.1$ m. Various grid discretization ratios ($\Delta x/\Delta z$) were tested, and the results were not sensitive to these changes. The model is initialized with zero initial velocity and more dense fluid on the right side and less dense fluid on the left side of the domain separated by an interface with a finite thickness δ , where the density field is

$$\rho(x, y, z, t = 0) = \rho_{\min} + \frac{\Delta\rho}{2} \left(1 - \operatorname{erf} \left(\frac{x}{\delta} \right) \right), \quad (22)$$

where $\delta=0.01$ m is the width of the interface, $\rho_{\min}=1025.9525$ kg m⁻³ is the initial density on the left side of the domain, and $\Delta\rho$ is the density difference between the two fluids chosen such that the reduced gravity is equal to [3,52]

$$g' = g \frac{\Delta\rho}{\rho_0} = 0.01 \text{ m s}^{-2}. \quad (23)$$

The model is run with a time step of $\Delta t=0.01$ s for a total of 180 s and free-slip boundary conditions at the walls. This choice of Δt was made after conducting a sensitivity analysis. With larger values of Δt , overturning billows were still observed, but details were more diffused. The temperature diffusivity is set to zero.

Fig. 5 shows the evolution of the exchange of the two different density fluids. The development and growth of a train of Kelvin–Helmholtz (KH) billows is evident. These characteristically nonhydrostatic features and vortical structures, which are not resolved in hydrostatic models (cf. [3]), develop when the velocity shear between the two layers exceeds the restoring force of stratification. More formally, these shear instabilities require that the gradient Richardson number be less than a critical value of 0.25 for sufficient periods of time.

For comparison with theory and prior studies, the front speed was calculated by tracking the position of the front over time along the bottom of the domain (i.e., $u_f = -dx_1^f/dt$ where x_1^f denotes the horizontal position of front along the bottom of the domain and the negative sign accounts for the leftward propagating front, cf. Härtel et al. [52]). The calculated front speed is compared to the buoyancy velocity, $u_b = \sqrt{g'D/2} = 0.0224$ m s⁻¹, using the nondimensional Froude number, $Fr = u_f/u_b$ [3,52].

The median Froude number over time of our experiment was equal to 0.7176, which is within 1.0% of the theoretical value of $1/\sqrt{2} = 0.7071$ originally formulated by Benjamin [53]. Moreover, this result compares well with the DNS results of Härtel et al. [52] ($Fr=0.675$, 4.5% error relative to theory) and the two-dimensional results of Fringer et al. [3] ($Fr=0.654$, 7.5% error relative to theory). Note that hydrostatic models tend to significantly underestimate the front speed relative to nonhydrostatic models [3]. Additionally, the Froude number has been shown to vary slightly with the Reynolds number (or the Grashof number) [52]. Nonetheless, the GCCOM model results are well within the range of error of other nonhydrostatic models and accurately capture the nonhydrostatic overturning billows.

Conservation of energy is also examined by tracking the total mechanical energy (TE) of the system over time, which is comprised of the potential energy (PE) and kinetic energy (KE)

$$TE = PE + KE = \int_{-L_x/2}^{L_x/2} \int_0^{L_y} \int_0^D \rho g z \, dx \, dy \, dz + \int_{-L_x/2}^{L_x/2} \int_0^{L_y} \int_0^D \frac{1}{2} \rho (u^2 + v^2 + w^2) \, dx \, dy \, dz. \quad (24)$$

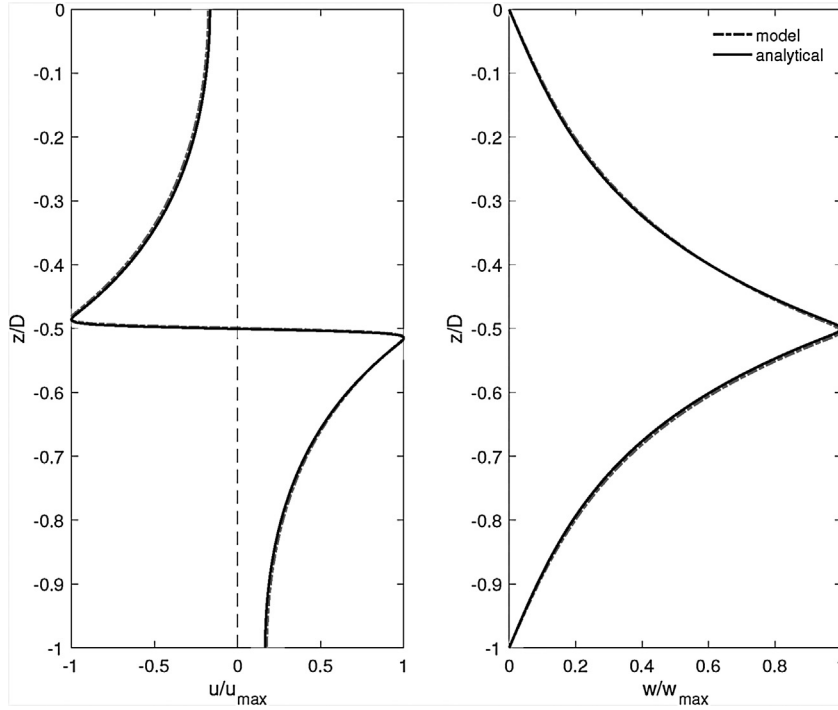


Fig. 4. Vertical profiles of the horizontal (left) and vertical (right) velocities at $t = 49$ s (maximum horizontal velocity) for $\epsilon = 1.6$ (dashed gray line). Analytical solutions to the first-mode linearized eigenfunction analysis of Fringer and Street [51] are also shown for reference (solid black line). Velocities are normalized by the maximum velocity for each respective profile.

Initially, the fluid is at rest so $KE|_{t=0} = 0$ and the TE in the system is comprised of PE,

$$PE|_{t=0} = g \frac{(\rho_{\max} + \rho_{\min})}{2} \frac{D^2}{2} L_y L_x. \quad (25)$$

Fig. 6 shows the evolution of TE in the system over time, as well as the partition between KE and PE which are in concordance with Lai et al. [27]. The total energy is normalized by the initial total energy in the system at $t = 0$. As the lock is released, the KE increases from zero and the PE decreases. As the front reaches the sidewalls, the KE decreases and the PE increases as the return flow develops. This transfer of energy between KE and PE continues as the front sloshes back and forth, although with decreasing magnitude. The total mechanical energy within the system is conserved to first order, with minimal energy loss due to viscous effects.

3.3. Field-scale internal wave beams

This final test case consists of the generation of internal wave beams in a continuously stratified fluid from an oscillatory flow over a Gaussian ridge. This field-scale test case follows the experimental setup of Vitousek and Fringer [6]. The simulation is performed in a domain ($128 \times 6 \times 101$) with a length of $L_x = 3000$ m and a depth of $D_0 = 1000$ m. In the center of the domain is a Gaussian ridge given by

$$D = D_0 - a_b \exp(-x^2/2L_b^2), \quad (26)$$

where the sill amplitude is $a_b = 20$ m and $L_b = L_x/100$ m.

The numerical simulation is initialized with a constant stratification of $N = 0.007 \text{ s}^{-1}$, where the buoyancy frequency squared is given by

$$N^2 = (-g/\rho_0) \partial \rho / \partial z. \quad (27)$$

This constant stratification corresponds to a linearly varying density with $\partial \rho / \partial z = -0.005 \text{ kg m}^{-4}$. The initial setup is shown in Fig. 7.

At the boundaries, the model is forced with an oscillatory tidal flow given by

$$u_{bc} = u_0 \sin(\omega t), \quad (28)$$

where $u_0 = 0.01 \text{ m s}^{-1}$. The model also uses sponge layers (SL) at the boundaries to minimize internal wave reflection, following the approach of Vitousek and Fringer [6],

$$SL(x, y, z, t) = -\frac{u(x, y, z, t) - u_{bc}(x, y, z, t)}{\tau_s} sl(r), \quad (29)$$

where $sl(r) = \exp(-4r/L_{sl})$, r is the distance to the domain boundary, and the damping time scale is $\tau_s = 100$ s. This allows the sponge layer to decay over the distance $L_{sl} = L_x/10$ [6].

In a fluid with constant stratification, forcing frequency ω , and in the absence of the Coriolis force (i.e., $f = 0$), internal wave beams will radiate with a constant slope given by the angle

$$\varphi = \tan^{-1} \left(\sqrt{\frac{(\omega/N)^2}{1 - (\omega/N)^2}} \right). \quad (30)$$

When $\omega/N \ll 1$, the nonhydrostatic beam angle approaches the hydrostatic beam angle given by

$$\varphi_h = \tan^{-1}(\omega/N). \quad (31)$$

In this test case, the forcing frequency ω is varied in different runs, while fixing the buoyancy frequency N such that $\omega/N = 0.2, 0.4, 0.6$, and 0.8 , respectively, for the various runs.

For all cases, the model is run with a time step of $\Delta t = 0.01$ s for a total time of 20 tidal periods ($T = 2\pi/\omega$) to enable sufficient spin-up time for the development of beams and to allow for transients to decay [6]. The beam angle was determined following Vitousek and Fringer [6] by finding the vertical location of the maximum of the root-mean-square velocity over the last ten tidal periods and in a limited horizontal region of [200, 500] m. A linear least-squares fit

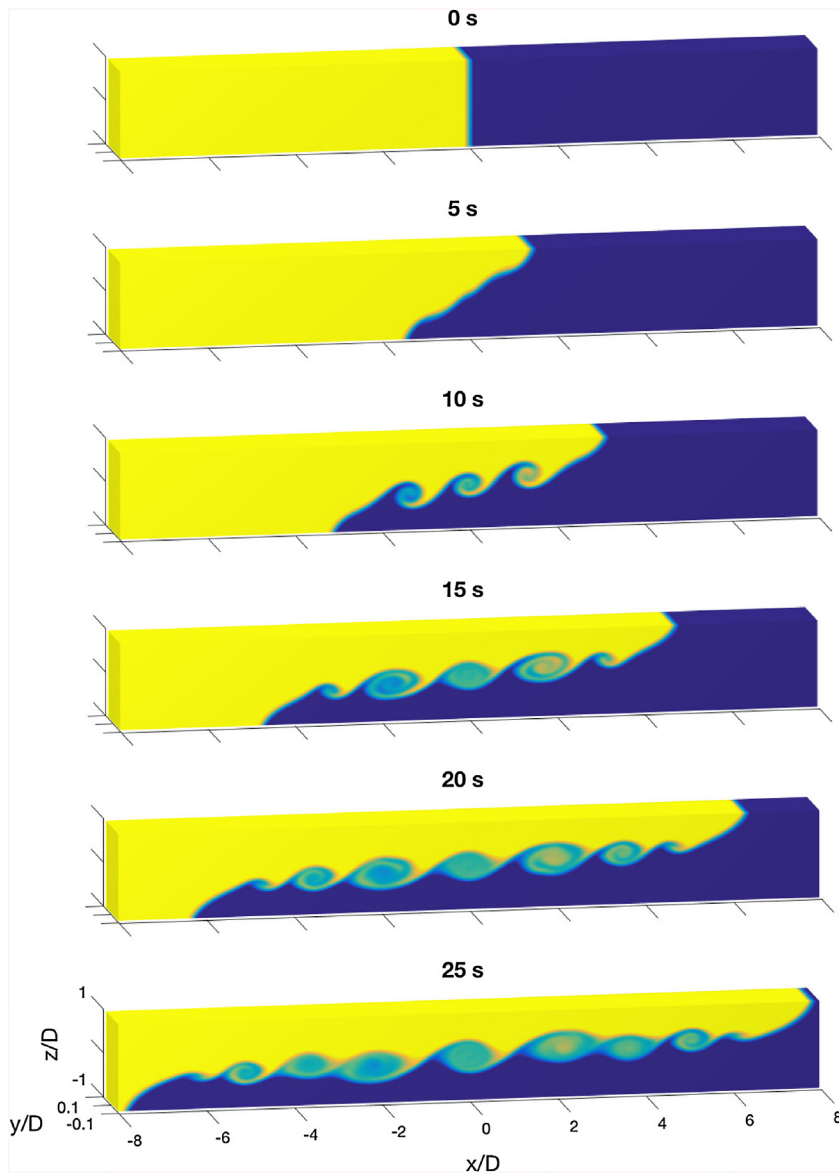


Fig. 5. Evolution of the lock exchange at different times. Shown is the non-dimensional density field over the three-dimensional domain.

to the $x-z$ location of these maxima was used to determine the internal wave beam angle.

Fig. 8 shows the horizontal velocity field normalized by the tidal velocity amplitude (u/u_0) for the various ω/N values considered. The flow field is shown after 19.5 tidal periods ($t = 19.5T$), corresponding to when $u_{bc} = 0$. Also shown are beam angles predicted by hydrostatic (Eq. (31)) and nonhydrostatic (Eq. (30)) theory. In all cases, the model produces internal wave beams that match the nonhydrostatic theory. This is particularly evident for large ω/N values, where nonhydrostatic effects are strongest. In this case, the hydrostatic theory predicts smaller angles compared to the nonhydrostatic theory and model results.

Fig. 9 shows the internal wave beam angle ϕ as a function of ω/N for the different model runs (as computed using the linear regression), as well as the angles predicted by hydrostatic and nonhydrostatic theory. The model is able to accurately capture the nonhydrostatic beam angle for all ω/N values considered. This test case demonstrates the ability of the model to accurately capture the proper internal wave behavior for this field-scale model.

4. Conclusions and future directions

GCCOM has previously been validated for idealized homogeneous environments, showcasing the advantages of its three-dimensional curvilinear coordinate system [54,34,35]. The version of the model described here computes the effects of density stratification by removing the buoyancy term and adding a horizontal pressure gradient force that arises from the hydrostatic component of pressure following Shchepetkin and McWilliams [38]. This representation more accurately captures gravity-driven flows and internal waves. The following numerical experiments are performed to demonstrate the abilities of the model: an internal seiche, a lock exchange (i.e., a lock release) in a rectangular tank, and internal wave beams generated from flow over a seamount. These test cases have been widely used as benchmarks for assessing the accuracy and efficiency of different nonhydrostatic numerical models.

For a small-amplitude internal seiche in a closed rectangular basin, GCCOM was able to accurately capture the wave speed for large aspect ratios, where nonhydrostatic effects are expected to be large, as well as the accurate decay of the velocity field away from the internal interface [21,3,6]. For the lock exchange experi-

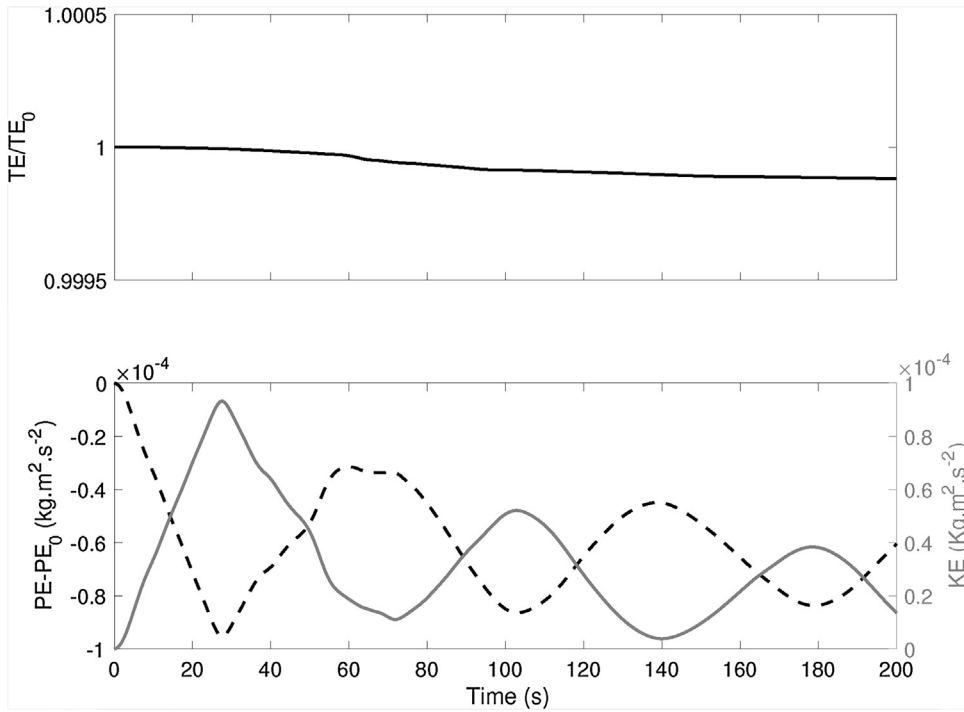


Fig. 6. (Top) Time series of total mechanical energy (potential plus kinetic) normalized by the initial total mechanical energy. (Bottom) Time series of potential energy (PE, dashed black line, left axis) and kinetic energy (KE, solid gray line, right axis), where the potential energy is shown as potential energy minus the initial potential energy to visualize on a similar scale as the kinetic energy.

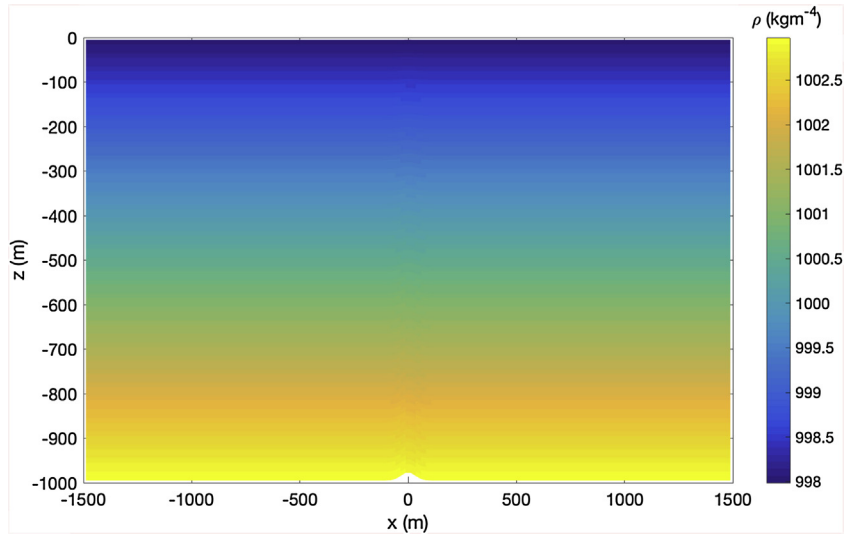


Fig. 7. Model configuration highlighting the initial density distribution with constant stratification. The Gaussian ridge is shown as solid white near the bottom.

ment, which is one of the most widely used test cases for validation [3,55,52,27], GCCOM was able to capture the characteristically nonhydrostatic overturning billows and propagation of the gravity current front. The Froude number of the front calculated from the GCCOM model showed excellent agreement relative to theory and other nonhydrostatic models. GCCOM also displayed the correct energetics and exchange between potential and kinetic energy throughout this experiment with minimal total energy loss. The last experiment considered the generation of internal waves by an oscillating tidal flow over a ridge in a continuously stratified fluid (similar to Chalamalla et al. [24], Jalali et al. [56], Kanarska et al. [7], Santilli and Scotti [5], Vitousek and Fringer [6]). GCCOM was able to accurately capture the nonhydrostatic beam angle predicted by

theory, particularly at large ω/N , where nonhydrostatic effects are most significant.

The vertical coordinate system is often reported as one of the critical aspects in the design of ocean models (see Vitousek and Fringer [6] and the references therein, and Haney [57], Berntsen [58]). One of the advantages of the GCCOM model is its general curvilinear coordinate system, which is capable of handling curvilinear orthogonal and non-orthogonal grids in all three dimensions (i.e., including the vertical dimension). This allows for the more accurate simulation of small-scale ocean process along very steep slopes (e.g., internal wave shoaling on a steep slope), as well as the flexibility to distribute the grid nodes along the vertical line in order to reduce the grid-induced errors [20]. General curvi-

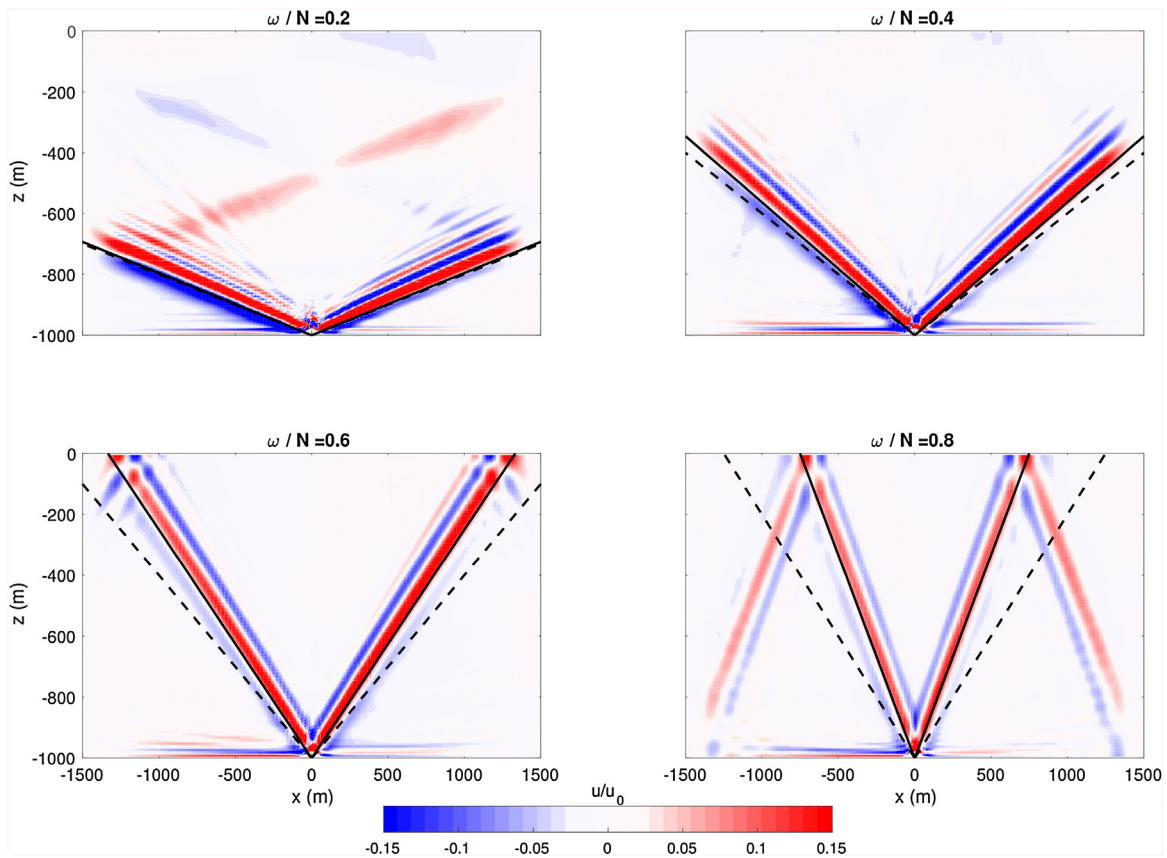


Fig. 8. Instantaneous horizontal velocity normalized by the tidal velocity amplitude (u/u_0) at $t = 19.5T$, corresponding to when $u_{bc} = 0$. Each plot corresponds to $\omega/N = 0.2, 0.4, 0.6$, and 0.8 for the top left, top right, bottom left, and bottom right, respectively. The theoretical beam angles predicted for hydrostatic (dashed black line) and nonhydrostatic (solid black line) theory are also shown.

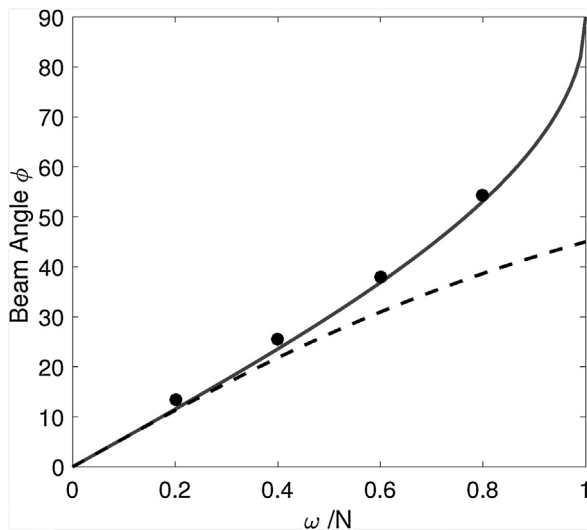


Fig. 9. Internal wave beam angle as a function of the forcing frequency nondimensionalized by the buoyancy frequency (ω/N). The model results are shown as solid black dots, and the angles predicted by hydrostatic and nonhydrostatic theory are shown as dashed and solid black lines, respectively.

linear coordinates are quite common in industrial and practical fluid dynamics applications where complex geometries strongly influence flows [59–61]; however, for ocean applications, relatively little is known about how this coordinate system can reduce model errors. In future work, the full 3D curvilinear coordinate system will be implemented, and tests will be conducted on real

bathymetry with nontrivial, realistic topography. Verification that the baroclinic pressure gradient force remains accurate over steep bathymetry will be tested, and this will be followed up with field-scale experiments of internal waves shoaling on a steep shelf. The realistic field-scale simulations will be compared with high-resolution field measurements of shoaling internal waves for verification [12,14,15].

Ongoing work with GCCOM includes a GCCOM PETSc-based parallel model, which has been re-designed using a data management distributed array (DMDA) domain decomposition strategy. This allows the Arakawa three-dimensional mesh to be easily divided among processors to improve performance. This parallel implementation was tested for accuracy and performance and some of the preliminary results can be found in Patel [62]. Future work will also focus on nesting a high-resolution nonhydrostatic GCCOM model within a larger-scale hydrostatic model (e.g., ROMS) for more efficient simulations of multiscale processes (cf. Choboter et al. [42]). Additionally, while the rigid lid approach for the immediate application of the modeling of field-scale internal waves is sufficient, future applications may require the implementation of a free-surface model which is more difficult to implement (e.g., metric terms in coordinate transformation are time-dependent) and more computationally expensive. With the goal of making GCCOM a user-friendly community model, a Cyber-infrastructure Web Application Framework (CyberWeb) [63,64] is being developed, through which scientists can run customized simulations, view results, and download data through a community portal.

Overall this paper presents a three-dimensional nonhydrostatic model for simulating small-scale processes in stratified flows. The model uses a fractional step algorithm for the computation of the

nonhydrostatic pressure, which accurately computes the density effects by adding a horizontal pressure gradient force. Benchmark test cases demonstrate that the model is capable of capturing non-hydrostatic behavior for gravity-driven flows and internal waves with excellent accuracy. Future studies will utilize the model capabilities for field-scale internal wave simulations.

Acknowledgments

We acknowledge the help of Mary Thomas, Manuel Valera, and Neelam Patel for their contribution to the development of the current GCCOM model. We also acknowledge helpful conversations with S. Vitousek on the internal wave beam experiments and the internal seiche modal analysis. We are especially grateful for the helpful comments and suggestions from three anonymous reviewers. Support was provided by the CSU Council on Ocean Affairs, Science and Technology (COAST) Grant Development Program. This research was supported by the Computational Science Research Center (CSRC) at San Diego State University (SDSU). The model data generated in this study are available at <http://dolphinsdsu.edu:8080/web-data/publ.3.2018/>.

Appendix A. Curvilinear coordinates transformation

Prior to the finite-difference discretization, the equations of motions (Eqs. (1)–(9)) are transformed into a uniform curvilinear grid (i.e., from (x, y, z) to (ξ, η, ζ) , Torres et al. [35]), in order to give the model the capability to perform calculations on three-dimensional arbitrarily shaped geometries. In the present work, all simulations are conducted in sigma coordinates. The following generalized independent variables are introduced

$$\tau = t, \quad \xi = \xi(x, y, z, t), \quad \eta = \eta(x, y, z, t), \quad \zeta = \zeta(x, y, z, t), \quad (\text{A.1})$$

where the derivatives transform according to

$$\frac{\partial}{\partial x} = \frac{\partial \xi}{\partial x} \frac{\partial}{\partial \xi} + \frac{\partial \eta}{\partial x} \frac{\partial}{\partial \eta} + \frac{\partial \zeta}{\partial x} \frac{\partial}{\partial \zeta}, \quad (\text{A.2})$$

$$\frac{\partial}{\partial y} = \frac{\partial \xi}{\partial y} \frac{\partial}{\partial \xi} + \frac{\partial \eta}{\partial y} \frac{\partial}{\partial \eta} + \frac{\partial \zeta}{\partial y} \frac{\partial}{\partial \zeta}, \quad (\text{A.3})$$

$$\frac{\partial}{\partial z} = \frac{\partial \xi}{\partial z} \frac{\partial}{\partial \xi} + \frac{\partial \eta}{\partial z} \frac{\partial}{\partial \eta} + \frac{\partial \zeta}{\partial z} \frac{\partial}{\partial \zeta}. \quad (\text{A.4})$$

The Jacobian of the transformation is defined as

$$J = \begin{vmatrix} \frac{\partial \xi}{\partial x} & \frac{\partial \xi}{\partial y} & \frac{\partial \xi}{\partial z} \\ \frac{\partial \eta}{\partial x} & \frac{\partial \eta}{\partial y} & \frac{\partial \eta}{\partial z} \\ \frac{\partial \zeta}{\partial x} & \frac{\partial \zeta}{\partial y} & \frac{\partial \zeta}{\partial z} \end{vmatrix}. \quad (\text{A.5})$$

A general rule for the derivatives can be defined as follows:

$$\begin{aligned} \xi_x &= J (y_\eta z_\zeta - y_\zeta z_\eta), & \eta_x &= J (y_\zeta z_\xi - y_\xi z_\zeta), & \zeta_x &= J (y_\xi z_\eta - y_\eta z_\xi), \\ \xi_y &= J (x_\zeta z_\eta - x_\eta z_\zeta), & \eta_y &= J (x_\xi z_\zeta - x_\zeta z_\xi), & \zeta_y &= J (x_\eta z_\xi - x_\xi z_\eta), \\ \xi_z &= J (x_\eta y_\zeta - x_\zeta y_\eta), & \eta_z &= J (x_\zeta y_\xi - x_\xi y_\zeta), & \zeta_z &= J (x_\xi y_\eta - x_\eta y_\xi). \end{aligned} \quad (\text{A.6})$$

Several keys aspects in the curvilinear coordinates transformation described above are noteworthy. First, the equations are transformed from the physical grid to a unit cube and the calculation is performed in that domain. Additionally, only the equations are transferred and not the variables. Finally, central

finite-differences are used to calculate the metrics of transformation, except at the boundaries, where forward or backward second order accurate finite-differences are used.

Appendix B. Numerical solution of Navier–Stokes in curvilinear coordinates

The GCCOM model uses a finite-difference scheme that is second order accurate in space [54]. For the linear terms, central differences are employed. The 4th-order accurate Kawamura method is used for the non-linear terms [47], for example

$$\left(f_\xi \frac{\partial u}{\partial \xi} \right)_{i,j,k} = \left| (f_\xi)_{i,j,k} \right| \frac{u_{i+2,j,k} - 4u_{i+1,j,k} + 6u_{i,j,k} + u_{i-2,j,k}}{4\delta\xi} \quad (\text{B.1})$$

where $f_\xi = u\xi_x + v\xi_y + w\xi_z$, and a similar formulation for the other non-linear terms. This discretization is similar to a central difference, but it is composed of both a forward and backward scheme, and its value changes depending on the sign of f_ξ .

Appendix C. Nonhydrostatic pressure in curvilinear coordinates

Calculating the nonhydrostatic pressure (Eq. (9)) requires discretizing the Laplacian

$$\nabla^2 p = \frac{\partial^2 p}{\partial x^2} + \frac{\partial^2 p}{\partial y^2} + \frac{\partial^2 p}{\partial z^2}. \quad (\text{C.1})$$

The Laplacian is expressed in curvilinear coordinates as follows [36]:

$$\begin{aligned} \nabla^2 p &= L(p) \left[\xi_x \frac{\partial p}{\partial \xi} + \eta_x \frac{\partial p}{\partial \eta} + \zeta_x \frac{\partial p}{\partial \zeta} \right] \\ &\quad - L(y) \left[\xi_y \frac{\partial p}{\partial \xi} + \eta_y \frac{\partial p}{\partial \eta} + \zeta_y \frac{\partial p}{\partial \zeta} \right] \\ &\quad - L(z) \left[\xi_z \frac{\partial p}{\partial \xi} + \eta_z \frac{\partial p}{\partial \eta} + \zeta_z \frac{\partial p}{\partial \zeta} \right], \end{aligned} \quad (\text{C.2})$$

where the components $L(p)$, $L(x)$, $L(y)$, $L(z)$ are written as

$$\begin{aligned} L(p) &= a \frac{\partial^2 p}{\partial \xi^2} + b \frac{\partial^2 p}{\partial \eta^2} + c \frac{\partial^2 p}{\partial \zeta^2} + 2 \left[d \frac{\partial^2 p}{\partial \xi \partial \eta} + e \frac{\partial^2 p}{\partial \zeta \partial \eta} + q \frac{\partial^2 p}{\partial \xi \partial \zeta} \right] \\ L(x) &= a \frac{\partial^2 x}{\partial \xi^2} + b \frac{\partial^2 x}{\partial \eta^2} + c \frac{\partial^2 x}{\partial \zeta^2} + 2 \left[d \frac{\partial^2 x}{\partial \xi \partial \eta} + e \frac{\partial^2 x}{\partial \zeta \partial \eta} + q \frac{\partial^2 x}{\partial \xi \partial \zeta} \right] \\ L(y) &= a \frac{\partial^2 y}{\partial \xi^2} + b \frac{\partial^2 y}{\partial \eta^2} + c \frac{\partial^2 y}{\partial \zeta^2} + 2 \left[d \frac{\partial^2 y}{\partial \xi \partial \eta} + e \frac{\partial^2 y}{\partial \zeta \partial \eta} + q \frac{\partial^2 y}{\partial \xi \partial \zeta} \right] \\ L(z) &= a \frac{\partial^2 z}{\partial \xi^2} + b \frac{\partial^2 z}{\partial \eta^2} + c \frac{\partial^2 z}{\partial \zeta^2} + 2 \left[d \frac{\partial^2 z}{\partial \xi \partial \eta} + e \frac{\partial^2 z}{\partial \zeta \partial \eta} + q \frac{\partial^2 z}{\partial \xi \partial \zeta} \right] \end{aligned} \quad (\text{C.3})$$

where a, b, c, d, e, q are defined as

$$\begin{aligned} a &= \xi_x^2 + \xi_y^2 + \xi_z^2, \\ b &= \eta_x^2 + \eta_y^2 + \eta_z^2, \\ c &= \zeta_x^2 + \zeta_y^2 + \zeta_z^2, \\ d &= \xi_x \eta_x + \xi_y \eta_y + \xi_z \eta_z, \\ e &= \zeta_x \eta_x + \zeta_y \eta_y + \zeta_z \eta_z, \\ q &= \xi_x \zeta_x + \xi_y \zeta_y + \xi_z \zeta_z. \end{aligned} \quad (\text{C.4})$$

Eq. (C.2) is solved using a cell-centered finite-difference method, where each term of the equation is discretized as follows:

$$\frac{\partial p}{\partial \xi} = (p_{(i+1,j,k)} - p_{(i-1,j,k)})/2\Delta_{\xi},$$

$$\frac{\partial p}{\partial \eta} = (p_{(i,j+1,k)} - p_{(i,j-1,k)})/2\Delta_{\eta}, \quad (\text{C.5})$$

$$\frac{\partial p}{\partial \zeta} = (p_{(i,j,k+1)} - p_{(i,j,k-1)})/2\Delta_{\zeta},$$

$$\frac{\partial^2 p}{\partial \xi^2} = (p_{(i+1,j,k)} + p_{(i-1,j,k)} - 2p_{(i,j,k)})/\Delta_{\xi}^2,$$

$$\frac{\partial^2 p}{\partial \eta^2} = (p_{(i,j+1,k)} + p_{(i,j-1,k)} - 2p_{(i,j,k)})/\Delta_{\eta}^2, \quad (\text{C.6})$$

$$\frac{\partial^2 p}{\partial \zeta^2} = (p_{(i,j,k+1)} + p_{(i,j,k-1)} - 2p_{(i,j,k)})/\Delta_{\zeta}^2,$$

$$\frac{\partial^2 p}{\partial \xi \partial \eta} = \frac{p_{(i+1,j+1,k)} + p_{(i-1,j-1,k)} - p_{(i+1,j-1,k)} - p_{(i-1,j+1,k)}}{4\Delta_{\xi}\Delta_{\eta}},$$

$$\frac{\partial^2 p}{\partial \xi \partial \zeta} = \frac{p_{(i+1,j,k+1)} + p_{(i-1,j,k-1)} - p_{(i+1,j,k-1)} - p_{(i-1,j,k+1)}}{4\Delta_{\xi}\Delta_{\zeta}},$$

$$\frac{\partial^2 p}{\partial \eta \partial \zeta} = \frac{p_{(i,j+1,k+1)} + p_{(i,j-1,k-1)} - p_{(i,j+1,k-1)} - p_{(i,j-1,k+1)}}{4\Delta_{\eta}\Delta_{\zeta}}. \quad (\text{C.7})$$

By substituting (C.5)–(C.7) into Eqs. (C.2) and (C.3), discretized curvilinear coordinates for use in the Poisson equation and the following expression are obtained:

$$\nabla^2 p = -\frac{1}{2(\Delta_{\xi}^2 \Delta_{\eta}^2 \Delta_{\zeta}^2)} \left\{ \begin{aligned} &4\alpha(i,j,k)p(i,j,k) \\ &+[\beta_1(i,j,k) + \beta_2(i,j,k)]p(i+1,j,k) \\ &+[\beta_1(i,j,k) - \beta_2(i,j,k)]p(i-1,j,k) \\ &+[\lambda_1(i,j,k) + \lambda_2(i,j,k)]p(i,j+1,k) \\ &+[\lambda_1(i,j,k) - \lambda_2(i,j,k)]p(i,j-1,k) \\ &+[\tau_1(i,j,k) + \tau_2(i,j,k)]p(i,j,k+1) \\ &+[\tau_1(i,j,k) - \tau_2(i,j,k)]p(i,j,k-1) \\ &+ \tau_{xy}(i,j,k)p(i+1,j-1,k) \\ &- \tau_{xy}(i,j,k)p(i+1,j+1,k) \\ &+ \tau_{xy}(i,j,k)p(i-1,j+1,k) \\ &- \tau_{xy}(i,j,k)p(i-1,j-1,k) \\ &+ \tau_{yz}(i,j,k)p(i,j+1,k-1) \\ &- \tau_{yz}(i,j,k)p(i,j+1,k+1) \\ &- \tau_{yz}(i,j,k)p(i,j-1,k-1) \\ &+ \tau_{yz}(i,j,k)p(i,j-1,k+1) \\ &- \tau_{xz}(i,j,k)p(i-1,j,k-1) \\ &+ \tau_{xz}(i,j,k)p(i-1,j,k+1) \\ &+ \tau_{xz}(i,j,k)p(i+1,j,k-1) \\ &- \tau_{xz}(i,j,k)p(i+1,j,k+1) \end{aligned} \right\} \quad (\text{C.8})$$

where α , β_1 , β_2 , λ_1 , λ_2 , τ_1 , τ_2 , τ_{xy} , τ_{yz} , τ_{xz} are transformation coefficients found after algebraic manipulation [65]. The corresponding coefficients are:

$$\alpha_{(i,j,k)} = (ac(i,j,k)\Delta_{\eta}^2\Delta_{\zeta}^2 + bc(i,j,k)\Delta_{\xi}^2\Delta_{\zeta}^2 + cc(i,j,k)\Delta_{\xi}^2\Delta_{\eta}^2), \quad (\text{C.9})$$

$$\beta_{1(i,j,k)} = -2ac(i,j,k)\Delta_{\eta}^2\Delta_{\zeta}^2, \quad (\text{C.10})$$

$$\beta_{2(i,j,k)} = L_{xc}(i,j,k)ixc(i,j,k) + L_{yc}(i,j,k)iyc(i,j,k) \\ + L_{zc}(i,j,k)izc(i,j,k)(\Delta_{\xi}^2\Delta_{\eta}^2\Delta_{\zeta}^2), \quad (\text{C.11})$$

$$\lambda_{1(i,j,k)} = -2bc(i,j,k) (\Delta_{\xi}^2\Delta_{\zeta}^2), \quad (\text{C.12})$$

$$\lambda_{2(i,j,k)} = (L_{xc}(i,j,k)jxc(i,j,k) + L_{yc}(i,j,k)jyc(i,j,k) \\ + L_{zc}(i,j,k)jzc(i,j,k))(\Delta_{\xi}^2\Delta_{\eta}^2\Delta_{\zeta}^2), \quad (\text{C.13})$$

$$\tau_{1(i,j,k)} = -2cc(i,j,k)(\Delta_{\xi}^2\Delta_{\eta}^2), \quad (\text{C.14})$$

$$\tau_{2(i,j,k)} = (L_{xc}(i,j,k)kxc(i,j,k) + L_{yc}(i,j,k)kyc(i,j,k) \\ + L_{zc}(i,j,k)kzc(i,j,k))(\Delta_{\xi}^2\Delta_{\eta}^2\Delta_{\zeta}^2), \quad (\text{C.15})$$

$$\tau_{xy}(i,j,k) = \Delta_{\xi}\Delta_{\eta}\Delta_{\zeta}^2 dc(i,j,k), \quad (\text{C.16})$$

$$\tau_{yz}(i,j,k) = \Delta_{\xi}^2\Delta_{\eta}\Delta_{\zeta} ec(i,j,k), \quad (\text{C.17})$$

$$\tau_{xz}(i,j,k) = \Delta_{\xi}\Delta_{\eta}^2\Delta_{\zeta} qc(i,j,k), \quad (\text{C.18})$$

where L_{xc} , L_{yc} , and L_{zc} represent $L(x)$, $L(y)$, and $L(z)$, respectively, discretized on the center grid according to (C.3). The terms ac , bc , cc , dc , qc are the discretized by the metric transformation in Eq. (C.4). The terms (ixc, iyc, izc) , (jxc, jyc, jzc) and (kxc, kyc, kzc) are the calculations of the derivative in the computational space represented in Eq. (A.6).

Eq. (C.2) is solved by obtaining a linear system of equations in the more standardized form:

$$A \hat{p} = \text{rhs}(\mathbf{u}) \quad (\text{C.19})$$

where $A \hat{p}$ is expressed explicitly in Eq. (C.8), and $\text{rhs}(\mathbf{u})$ is the discretization of the right-hand side of Eq. (9). The matrix A is not singular, is both large and sparse, and requires a 19-point stencil with coefficient values based on the chosen mesh shape.

In order to construct our 3D Laplacian operator, the set of points on the 3D curvilinear mesh are mapped as an ordered numerical set. This is achieved by imposing an ordering on the grid termed an imposed lexicographical order of the unknown $p(i,j,k)$. The natural row ordering at the interior points of the domain is illustrated in Fig. C.1, starting from bottom-to-top and continuing from left-to-right.

From here, a large number of algorithms are available for solving systems of equations with sparse matrices; depending on the given application, some algorithms perform better than others. Several methods are regularly used when solving time-dependent, incompressible Navier–Stokes equations, each with their own advantages and disadvantages. Direct methods based on Gaussian elimination solve small systems of equations efficiently; however, their work and memory requirements prohibit them from being used for very large systems. Conversely, multigrid methods [66] are well suited for problems featuring large numbers of unknowns. Furthermore, to lower the computational cost of the nonhydrostatic pressure in GGCOM, two libraries were integrated: the Aggregation-based Algebraic Multigrid Library (AGMG [39]) and the Portable Extensible Toolkit for Scientific Computation (PetSC [40]) a comparison of the efficiency of these libraries in GCCOM is presented in Valera et al. [41].

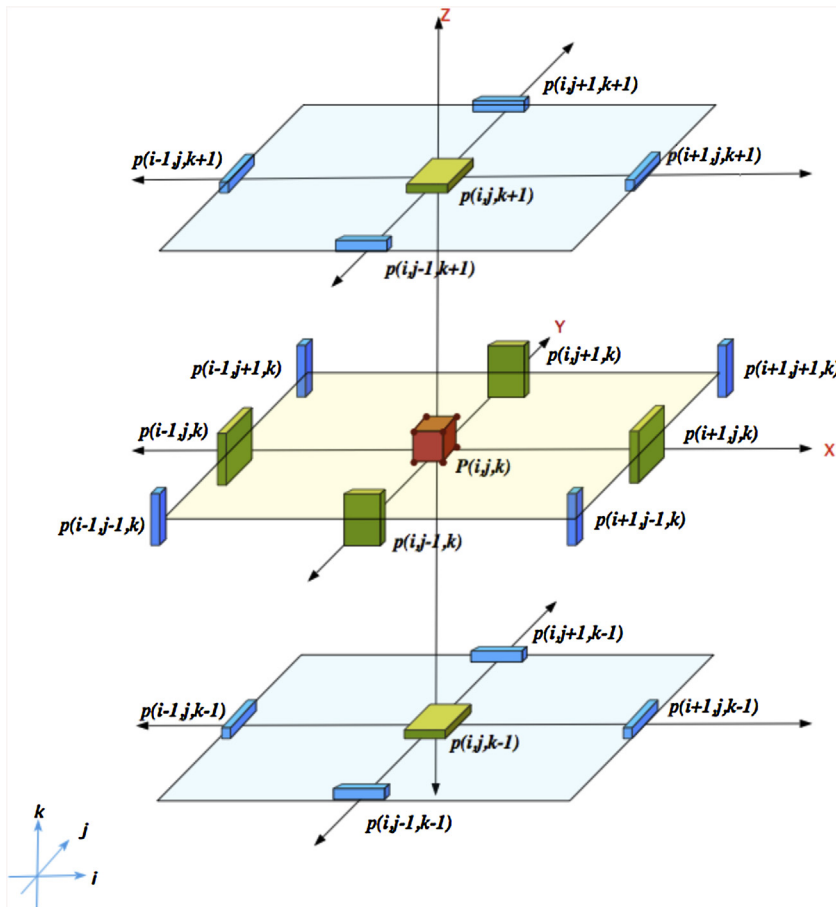


Fig. C.1. Lexicographical ordering for the Laplacian required to solve for pressure in curvilinear coordinates. Natural row ordering, from bottom-to-top and then from left-to-right. Figure from Garcia [65].

References

- [1] Y. Chao, J.D. Farrara, H. Zhang, K.J. Armenta, L. Centurioni, F. Chavez, J.B. Girton, D. Rudnick, R.K. Walter, Development, implementation, and validation of a California coastal ocean modeling, data assimilation, and forecasting system, *Deep Sea Res. Part II: Top. Stud. Oceanogr.* 151 (2018) 49–63, <http://dx.doi.org/10.1016/j.dsr2.2017.04.013>, *Studies of the California Current System Part 3*.
- [2] V. Casulli, A semi-implicit finite difference method for non-hydrostatic, free-surface flows, *Int. J. Numer. Methods Fluids* 30 (1999) 425–440, [http://dx.doi.org/10.1002/\(SICI\)1097-0363\(19990630\)30:4<425::AID-FLD847>3.0.CO;2-D](http://dx.doi.org/10.1002/(SICI)1097-0363(19990630)30:4<425::AID-FLD847>3.0.CO;2-D).
- [3] O.B. Fringer, J.C. McWilliams, R.L. Street, A new hybrid model for coastal simulations, *Oceanography* 19 (2006) 64–77.
- [4] J. Marshall, C. Hill, L. Perelman, A. Adcroft, Hydrostatic, quasi-hydrostatic, and nonhydrostatic ocean modeling, *Geophys. Res.* 102 (1997) 5733–5752.
- [5] E. Santilli, A. Scotti, The stratified ocean model with adaptive refinement (SOMAR), *J. Comput. Phys.* 291 (2015) 60–81, <http://dx.doi.org/10.1016/j.jcp.2015.03.008>.
- [6] S. Vitousek, O.B. Fringer, A nonhydrostatic, isopycnal-coordinate ocean model for internal waves, *Ocean Model.* 83 (2014) 118–144, <http://dx.doi.org/10.1016/j.ocemod.2014.08.008>.
- [7] Y. Kanarska, A. Shchepetkin, J.C. McWilliams, Algorithm for non-hydrostatic dynamics in the Regional Oceanic Modeling System, *Ocean Model.* 18 (2007) 143–174, <http://dx.doi.org/10.1016/j.ocemod.2007.04.001>.
- [8] J.J. Leichter, S.R. Wing, S.L. Miller, M.W. Denny, Pulsed delivery of subthermocline water to Conch Reef (Florida Keys) by internal tidal bores, *Limnol. Oceanogr.* 41 (1996) 1490–1501, <http://dx.doi.org/10.4319/lo.1996.41.7.1490>.
- [9] A.J. Lucas, P.J. Franks, C.L. Dupont, Horizontal internal-tide fluxes support elevated phytoplankton productivity over the inner continental shelf, *Limnol. Oceanogr.: Fluids Environ.* 1 (2011) 56–74, <http://dx.doi.org/10.1215/21573698-1258185>.
- [10] M. Noble, B. Jones, P. Hamilton, J. Xu, G. Robertson, L. Rosenfeld, J. Largier, Cross-shelf transport into nearshore waters due to shoaling internal tides in San Pedro Bay, CA, *Cont. Shelf Res.* 29 (2009) 1768–1785, <http://dx.doi.org/10.1016/j.csr.2009.04.008>.
- [11] M.M. Omand, J.J. Leichter, P.J.S. Franks, R.T. Guza, A.J. Lucas, F. Feddersen, Physical and biological processes underlying the sudden surface appearance of a red tide in the nearshore, *Limnol. Oceanogr.* 56 (2011) 787–801, <http://dx.doi.org/10.4319/lo.2011.56.3.0787>.
- [12] R.K. Walter, P.J. Phelan, Internal bore seasonality and tidal pumping of subthermocline waters at the head of the Monterey submarine canyon, *Cont. Shelf Res.* 116 (2016) 42–53, <http://dx.doi.org/10.1016/j.csr.2016.01.015>.
- [13] R.K. Walter, M. Stastna, C.B. Woodson, S.G. Monismith, Observations of nonlinear internal waves at a persistent coastal upwelling front, *Cont. Shelf Res.* 117 (2016) 100–117, <http://dx.doi.org/10.1016/j.csr.2016.02.007>.
- [14] R.K. Walter, C.B. Woodson, R.S. Arthur, O.B. Fringer, S.G. Monismith, Nearshore internal bores and turbulent mixing in southern Monterey Bay, *J. Geophys. Res.* 117 (2012) C07017, <http://dx.doi.org/10.1029/2012JC008115>.
- [15] R.K. Walter, C.B. Woodson, P.R. Leary, S.G. Monismith, Connecting wind-driven upwelling and offshore stratification to nearshore internal bores and oxygen variability, *J. Geophys. Res. Oceans* (2014) 1–18, <http://dx.doi.org/10.1002/2014JC009998>.
- [16] G.L. Wolanski, E. Pickard, Upwelling by internal tides and kelvin waves at the continental shelf break on the Great Barrier Reef, *Mar. Freshw. Res.* 34 (1983) 65–80, <http://dx.doi.org/10.1071/mf9830065>.
- [17] J. Berntsen, J. Xing, A.M. Davies, Numerical studies of flow over a sill: sensitivity of the non-hydrostatic effects to the grid size, *Ocean Dyn.* 59 (2009) 1043–1059, <http://dx.doi.org/10.1007/s10236-009-0227-0>.
- [18] J. Marshall, H. Jones, C. Hill, Efficient ocean modeling using non-hydrostatic algorithms, *J. Mar. Syst.* 18 (1998) 115–134.
- [19] S. Vitousek, O.B. Fringer, Physical vs. numerical dispersion in nonhydrostatic ocean modeling, *Ocean Model.* 40 (2011) 72–86, <http://dx.doi.org/10.1016/j.ocemod.2011.07.002>.
- [20] M. Abouali, J.E. Castillo, Unified Curvilinear Ocean Atmosphere Model (UCOAM): a vertical velocity case study, *Math. Comput. Model.* 57 (2013) 2158–2168, <http://dx.doi.org/10.1016/j.mcm.2011.03.023>.
- [21] C. Ai, W. Ding, A 3D unstructured non-hydrostatic ocean model for internal waves, *Ocean Dyn.* 66 (2016) 1253–1270, <http://dx.doi.org/10.1007/s10236-016-0980-9>.
- [22] J. Berntsen, J. Xing, G. Alendal, Assessment of non-hydrostatic ocean models using laboratory scale problems, *Cont. Shelf Res.* 26 (2006) 1433–1447.
- [23] D. Botelho, J. Imberger, C. Dallimore, B.R. Hodges, A hydrostatic/non-hydrostatic grid-switching strategy for computing

- high-frequency, high wave number motions embedded in geophysical flows, *Environ. Model. Softw.* 24 (2009) 473–488, <http://dx.doi.org/10.1016/j.envsoft.2008.09.008>.
- [24] V.K. Chalamalla, E. Santilli, A. Scotti, M. Jalali, S. Sarkar, SOMAR-LES: a framework for multi-scale modeling of turbulent stratified oceanic flows, *Ocean Model.* 120 (2017) 101–119, <http://dx.doi.org/10.1016/j.ocemod.2017.11.003>.
- [25] O.B. Fringer, M. Gerritsen, R.L. Street, An unstructured-grid, finite-volume, nonhydrostatic, parallel coastal ocean simulator, *Ocean Model.* 14 (2006) 139–173, <http://dx.doi.org/10.1016/j.ocemod.2006.03.006>.
- [26] S. Koltakov, O.B. Fringer, Moving grid method for numerical simulation of stratified flows, *Int. J. Numer. Methods Fluids* 71 (2013) 1524–1545, <http://dx.doi.org/10.1002/flid.3724>.
- [27] Z. Lai, C. Chen, G.W. Cowles, R.C. Beardsley, A nonhydrostatic version of FVCOM: 1. Validation experiments, *J. Geophys. Res. Oceans* 115 (2010) 1–23, <http://dx.doi.org/10.1029/2009JC005525>.
- [28] Z. Liu, L. Lin, L. Xie, H. Gao, Partially implicit finite difference scheme for calculating dynamic pressure in a terrain-following coordinate non-hydrostatic ocean model, *Ocean Model.* 106 (2016) 44–57, <http://dx.doi.org/10.1016/j.ocemod.2016.09.004>.
- [29] J. Marshall, A. Adcroft, C. Hill, L. Perelman, C. Heisey, A finite-volume, incompressible Navier Stokes model for studies of the ocean on parallel computers, *J. Geophys. Res. Oceans* 102 (1997) 5753–5766, <http://dx.doi.org/10.1029/96JC02775>.
- [30] K. Qu, H. Tang, A. Agrawal, C. Jiang, B. Deng, Evaluation of SIFOM-FVCOM system for high-fidelity simulation of small-scale coastal ocean flows, *J. Hydrodyn. Ser. B* 28 (2016) 994–1002.
- [31] G.S. Stelling, M. Zijlema, Numerical modeling of wave propagation, breaking and run-up on a beach, in: B. Koren, K. Vuik (Eds.), *Advanced Computational Methods in Science and Engineering*, Springer, Berlin, Heidelberg, 2010, pp. 373–401.
- [32] H. Theias, Numerical modeling of non-hydrostatic processes in estuarine and coastal regions, Master's thesis, MSc dissertation thesis, Technical University of Lisbon, Portugal, 2005 http://www.mohid.com/PublicData/products/Thesis/MSc_HernaniTheias2005.pdf.
- [33] C.R. Torres, H. Hanazaki, J. Ochoa, J. Castillo, M. Van Woert, Flow past a sphere moving vertically in a stratified diffusive fluid, *J. Fluid Mech.* 417 (2000) 211–236, <http://dx.doi.org/10.1017/S002211200001002>.
- [34] C.R. Torres, Modeling ocean circulation in boundary-fitted coordinates: the GCOM Project, III Pan-American Adv. Stud. Inst. Comput. Sci. Eng. (2006) 1–37.
- [35] C.R. Torres, A.S. Mascarenhas, J.E. Castillo, Three-dimensional stratified flow over Alarcón Seamount, Gulf of California entrance, Deep Sea Res. Part II: Top. Stud. Oceanogr. 51 (2004) 647–657, <http://dx.doi.org/10.1016/j.dsr2.2004.05.012>.
- [36] C.R. Torres, J.E. Castillo, Stratified rotating flow over complex terrain, *Appl. Numer. Math.* 47 (2003) 531–541, [http://dx.doi.org/10.1016/S0168-9274\(03\)00085-0](http://dx.doi.org/10.1016/S0168-9274(03)00085-0).
- [37] C.R. Torres, D. De Cecchis, G. Larrazabal, J. Castillo, Numerical study of a descending sphere in a low, *Electron. Trans. Numer. Anal.* 34 (2008) 1–7.
- [38] A.F. Shchepetkin, J.C. McWilliams, A method for computing horizontal pressure-gradient force in an oceanic model with a nonaligned vertical coordinate, *J. Geophys. Res.* 108 (2003) 3090, <http://dx.doi.org/10.1029/2001JC001047>.
- [39] Y. Notay, An aggregation-based algebraic multigrid method, *Electron. Trans. Numer. Anal.* 37 (2010) 123–146.
- [40] S. Balay, W.D. Gropp, L.C. McInnes, B.F. Smith, Efficient management of parallelism in object oriented numerical software libraries, in: E. Arge, A.M. Bruaset, H.P. Langtangen (Eds.), *Modern Software Tools in Scientific Computing*, Birkhäuser Press, 1997, pp. 163–202.
- [41] M. Valera, N. Patel, J. Castillo, PETSc-based parallelization of the fully 3D-curvilinear non-hydrostatic coastal ocean dynamics model, GCCOM, Technical Report CSRCR2017-02, Computational Sciences Research Center, San Diego State University, 2017 http://www.csrc.sdsu.edu/research_reports/CSRCR2017-02.pdf.
- [42] P.F. Choboter, M. Garcia, D.D. Cecchis, M. Thomas, R.K. Walter, J.E. Castillo, Nesting nonhydrostatic GCCOM within hydrostatic ROMS for multiscale coastal ocean modeling, *Oceans 2016 MTS/IEEE Monterey* (2016) 1–4, <http://dx.doi.org/10.1109/OCEANS.2016.7761488>.
- [43] M. Garcia, T. Hoar, M. Thomas, B. Bailey, J. Castillo, Interfacing an ensemble data assimilation system with a 3D nonhydrostatic coastal ocean model, an OSSE experiment, *Oceans 2016 MTS/IEEE Monterey* (2016) 1–11, <http://dx.doi.org/10.1109/OCEANS.2016.7760992>.
- [44] J. Smagorinsky, General circulation experiments with the primitive equations, *Mon. Weather Rev.* 91 (1963) 99, [http://dx.doi.org/10.1175/1520-0493\(1963\)091<0099:GCEWTP>2.3.CO;2](http://dx.doi.org/10.1175/1520-0493(1963)091<0099:GCEWTP>2.3.CO;2).
- [45] J.D. Albertson, M.B. Parlange, Surface length scales and shear stress: implications for land-atmosphere interaction over complex terrain, *Water Resour. Res.* 35 (1999) 2121–2132.
- [46] A.E. Gill, *Atmosphere-Ocean Dynamics*, Academic Press, 1982.
- [47] T. Kawamura, H. Takami, K. Kuwahara, Computation of high Reynolds number flow around a circular cylinder with surface roughness, *Fluid Dyn. Res.* 1 (1986) 145–162 http://iopscience.iop.org/1873-7005/1/2/A05/pdf/1873-7005_1_2_A05.pdf.
- [48] J. Kim, P. Moin, Application of a fractional-step method to incompressible Navier-Stokes equation, *J. Comput. Phys.* 59 (1985) 208–232.
- [49] L.J. Wicker, W.C. Skamarock, Time-splitting methods for elastic models using forward time schemes, *Mon. Weather Rev.* (2002) 2088–2097.
- [50] P. Kundu, *Fluid Mechanics*, Academic Press, 1999.
- [51] O.B. Fringer, R.L. Street, The dynamics of breaking progressive interfacial waves, *J. Fluid Mech.* 494 (2003) 319–353 <http://libproxy.sdsu.edu/login?url=https://search.proquest.com/docview/210903257?accountid=13758>.
- [52] C. Härtel, E. Meiburg, F. Necker, Analysis and direct numerical simulation of the flow at a gravity-current head. Part 1. Flow topology and front speed for slip and no-slip boundaries, *J. Fluid Mech.* 418 (2000) 189–212, <http://dx.doi.org/10.1017/S0022112000001221>.
- [53] T.B. Benjamin, Gravity currents and related phenomena, *J. Fluid Mech.* 31 (1968) 209–248, <http://dx.doi.org/10.1017/S0022112068000133>.
- [54] M. Abouali, J.E. Castillo, Solving Poisson equation with Robin boundary condition on a curvilinear mesh using high order mimetic discretization methods, *Math. Comput. Simul.* (2014), <http://dx.doi.org/10.1016/j.matcom.2014.10.004>.
- [55] C. Härtel, L. Kleiser, M. Michaud, C.F. Stein, A direct numerical simulation approach to the study of intrusion fronts, *J. Eng. Math.* 32 (1997) 103–120.
- [56] M. Jalali, N.R. Rapaka, S. Sarkar, Tidal flow over topography: effect of excitation number on wave energetics and turbulence, *J. Fluid Mech.* 750 (2014) 259–283, <http://dx.doi.org/10.1017/jfm.2014.258>.
- [57] R.L. Haney, On the pressure gradient force over steep topography in sigma coordinate ocean models, *J. Phys. Oceanogr.* 21 (1991) 610–619, [http://dx.doi.org/10.1175/1520-0485\(1991\)021<0610:OTPGFO>2.0.CO;2](http://dx.doi.org/10.1175/1520-0485(1991)021<0610:OTPGFO>2.0.CO;2).
- [58] J. Bernsten, Internal pressure errors in sigma-coordinate ocean models, *J. Atmos. Oceanic Technol.* 19 (2002) 1403–1414, [http://dx.doi.org/10.1175/1520-0426\(2002\)019<1403:IPESC>2.0.CO;2](http://dx.doi.org/10.1175/1520-0426(2002)019<1403:IPESC>2.0.CO;2).
- [59] S. Dey, R.M. O'Bara, M.S. Shephard, Curvilinear mesh generation in 3D, in: *Proceedings of the Eighth International Meshing Roundtable*, John Wiley and Sons, 1999, pp. 407–417.
- [60] S. Jordan, A large-eddy simulation methodology in generalized curvilinear coordinates, *J. Comput. Phys.* 148 (1999) 322–340, <http://dx.doi.org/10.1006/jcph.1998.6112>.
- [61] B. Panjwani, I.S. Ertesvag, A. Gruber, K.E. Rian, Large eddy simulation in generalized curvilinear coordinates using conventional approach: theory and validation, *Int. J. Numer. Methods Fluids* 69 (2012) 671–690, <http://dx.doi.org/10.1002/flid.2580>.
- [62] N.V. Patel, Validation of a PETSc-based parallel general curvilinear coastal ocean model, Master's thesis, San Diego State University, 2017 <http://libproxy.sdsu.edu/login?url=https://search.proquest.com/docview/1988186395?accountid=13758>.
- [63] M.P. Thomas, J. Burruss, L. Cinquini, G. Fox, D. Gannon, L. Gilbert, G.V. Laszewski, K. Jackson, D. Middleton, R. Moore, M. Pierce, B. Plale, A. Rajasekar, R. Regno, E. Roberts, D. Schissel, A. Seth, W. Schroeder, Grid portal architectures for scientific applications, *J. Phys. Conf. Ser.* 16 (2005) 596–600, <http://dx.doi.org/10.1088/1742-6596/16/1/083>.
- [64] M.P. Thomas, J.E. Castillo, Development of a computational environment for the General Curvilinear Ocean Model (GCCOM), *J. Phys. Conf. Ser.* 180 (2009).
- [65] M. Garcia, Data assimilation unit for the general curvilinear environmental model, 2015, – copyright – Database copyright ProQuest LLC; ProQuest does not claim copyright in the individual underlying works; Last updated – 2016-03-24 <http://libproxy.sdsu.edu/login?url=http://search.proquest.com/docview/1771299218?accountid=13758>.
- [66] S. Gratton, P.L. Toint, J. Tshimanga, Conjugate gradients versus multigrid solvers for diffusion-based correlation models in data assimilation, *Q. J. Roy. Meteor. Soc.* 139 (2013) 1481–1487, <http://dx.doi.org/10.1002/qj.2050>.



and oil spill tracking.

Mariangel Garcia is a Research Associate at the Computational Science Research Center at San Diego State University (SDSU) and a model developer of the General Curvilinear Coastal Ocean Model (GCCOM) at the Coastal Ocean Dynamics Group. She received her Ph.D. in Computational Science at Claremont Graduate University, a joint program with SDSU. Garcia holds a Licenciatura in Mathematics and M.Sc. in Stochastic Modeling. Her main research of interest is to develop a high-fidelity nonhydrostatic ocean model to study the propagation and breaking of internal waves over a shelf. Her research also involve Data Assimilation with focus in simulating coastal hydrodynamics, some applications include tsunamis simulation



Paul Choboter is a Professor in the Mathematics Department at California Polytechnic State University. He earned his Ph.D. in Applied Mathematics from the University of Alberta, his M.Sc. in Mathematics from McGill University, and his B.Sc. in Mathematical Physics from Simon Fraser University. Dr. Choboter is a member of Cal Poly's Center for Coastal Marine Science and the Coastal Ocean Dynamic Group at San Diego State University. His research interests include geophysical fluid dynamics and scientific computation.



Ryan Walter is Assistant Professor in the Physics Department at California Polytechnic State University. He earned his M.S. and Ph.D. in the Dept. of Civil and Environmental Engineering at Stanford University, and the B.S.E. in Civil and Environmental Engineering at Cornell University. His interests are in the field of environmental fluid mechanics, and involve the application of fluid dynamics principles to the study of flow and transport processes in coastal and estuarine systems.



Jose Castillo is director of the San Diego State University Computational Science Research Center. He has a wide range of interests in applied mathematics with emphasis in numerical solution of partial differential equations, scientific computing, and modeling. His numerical interests are mainly in the solution of partial differential equations in irregular geometries with emphasis on grid generation for both geometry and solution adaption. He has developed new grid generation algorithms based on intuitive discrete geometric notions and has built codes to implement these ideas. He has studied the underlying mathematics including existence and uniqueness, and smoothness properties of the variational problems. He has research projects involving High Order Finite Difference Schemes, Error analysis and Adaptive Grid Generation methods.